Electrostrain in excess of 1% in polycrystalline piezoelectrics

Bastola Narayan[1], Jaskaran Singh Malhotra[1], Rishikesh Pandey[1], Krishna Yaddanapudi[1], Pavan Nukala[2], Brahim Dkhil[2], Anatoliy Senyshyn [3] and Rajeev Ranjan [1]*

Piezoelectric actuators transform electrical energy into mechanical energy, and because of their compactness, quick response time and accurate displacement, they are sought after in many applications. Polycrystalline piezoelectric ceramics are technologically more appealing than single crystals due to their simpler and less expensive processing, but have yet to display electrostrain values that exceed 1%. Here we report a material design strategy wherein the efficient switching of ferroelectric–ferroelastic domains by an electric field is exploited to achieve a high electrostrain value of 1.3% in a pseudo-ternary ferroelectric alloy system, $BiFeO_3$–$PbTiO_3$–$LaFeO_3$. Detailed structural investigations reveal that this electrostrain is associated with a combination of several factors: a large spontaneous lattice strain of the piezoelectric phase, domain miniaturization, a low-symmetry ferroelectric phase and a very large reverse switching of the non-180° domains. This insight for the design of a new class of polycrystalline piezoceramics with high electrostrains may be useful to develop alternatives to costly single-crystal actuators.

High-performance piezoelectrics are used in a large variety of applications, such as ultrasonic transducers for medical imaging, high-precision actuation, guidance systems, the automotive industry and so on[1]. The most important parameter of a piezoelectric material regarding its use as an actuator is the strain induced by an electric field (also known as electrostrain). Single crystals of $Pb(Zn_{1/3}Nb_{2/3})O_3$–$PbTiO_3$ (PZN-PT) and $Pb(Mg_{1/3}Nb_{2/3})O_3$–$PbTiO_3$ (PMN-PT) have set the benchmark electrostrain at ~1.7% (ref. [2]). The growth of high-quality single crystals requires a delicate control of many different experimental parameters over a long period of time. A slight unintentional variation in any one of the experimental conditions, even for a short duration, can ruin the quality of the crystal and its intended property. In some cases, it is not possible to grow single crystals of the most-desired compositions[3]. As compared to the production of single crystals, the fabrication of non-textured polycrystalline piezoceramics is less time and energy consuming and can be produced in large quantities with reproducible properties. However, unlike single crystals wherein the best electrostrain can be tapped by orienting the crystal in a suitable direction, the response of a non-textured polycrystalline piezoceramic is an ensemble average of the property over all the possible orientations of the corresponding single crystal. The mutual clamping of the differently oriented grains also plays an important role in determining the piezoelectric response of polycrystalline piezoceramics[4,5]. The maximum electrostrain reported in polycrystalline piezoceramic is 0.7% which has been attributed to a cubic-like (CL)-to-rhombohedral transformation in a $Na_{1/2}Bi_{1/2}TiO_3$-based piezoceramic[6].

The grains of a polycrystalline piezoceramic are inevitably in a multidomain state to minimize the transformation stress as the ceramic body cools through the Curie point after undergoing densification at a high (sintering) temperature[7]. The electrostrain of a piezoceramic is determined primarily by the mechanism(s) associated with domain switching[5,7,8]. This situation contrasts with the single-crystal piezoelectrics, such as PZN-PT and PMN-PT, wherein the ultrahigh actuation is attributed to the polarization rotation induced by an electric-field in a monodomain and/or domain-engineered state[9,10]. In principle, a large electrostrain can be achieved if a ferroelectric material with a large spontaneous lattice strain also shows good domain switching. The tetragonal ferroelectrics $BaTiO_3$ (BT) and $PbTiO_3$ (PT) exhibit spontaneous lattice strains (c/a of ~1, where a and c are the tetragonal lattice parameters) of ~0.01 and ~0.06, respectively. If an electric field could convert all the a domains into c domains in a multidomain single crystal, one may anticipate the electrostrain to approach 1% and 6% in BT and PT, respectively. An electrostrain of 0.75% has been reported by domain switching in a multidomain crystal of BT[11]. If domain switching were equally easy in PT, an extraordinary electrostrain of ~6% should be realized. However, domain switching becomes increasingly difficult with an increasing magnitude of spontaneous lattice strain. Even if the domain switching can be significantly enhanced, the reproducibility of the large electrostrain in repeated cycles requires the material to have some inherent mechanism to restore the nearly random domain configuration when the field is switched off[11]. Such a possibility appears to exist in relaxor ferroelectrics, wherein the ferroelectric domains are miniaturized to the extent that they form polar nanoregions, and they coexist (and possibly compete) with ferroelectric domains of longer coherence lengths[12].

Material selection

We explored the possibility of realizing a large electrostrain by taking a ferroelectric material with giant tetragonality as a host and improving its domain switchability by chemical tuning. For this, we chose $(1–x)BiFeO_3$–$(x)PbTiO_3$ (BF-PT) as it exhibits a very large tetragonal spontaneous lattice strain (c/a –1) of 0.18 (refs [13,14]). This strain is three times that in PT (~0.06 (c/a –1)) and 18 times that in BT (~0.01 (c/a –1)). Chemical tuning of BF-PT was

[1]Department of Materials Engineering, Indian Institute of Science, Bangalore, India. [2]Laboratoire Structures, Propriétés et Modélisation des Solides (SPMS), CentraleSupélec, CNRS-UMR8580, Université Paris-Saclay, Gif-sur-Yvette, France. [3]Forschungsneutronenquelle Heinz Maier-Leibnitz (FRM II), Technische Universität München, Garching b. München, Germany. *e-mail: rajeev@iisc.ac.in
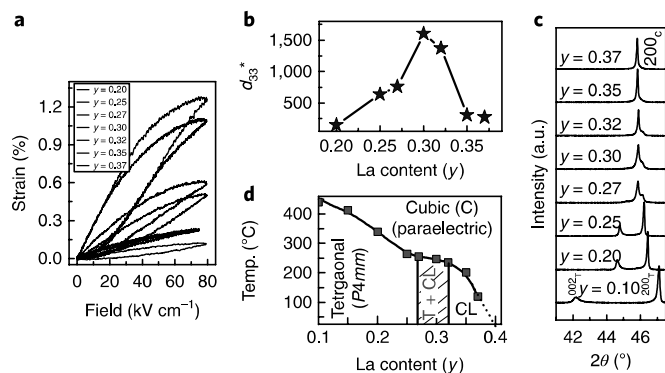
Fig. 1 | Structure–property correlation. a, Electric-field dependent unipolar strain of $0.55Bi_{1-y}La_yFeO_3$–$0.45PbTiO_3$ for different La concentration (y). **b**, d_{33}^* (the large-signal piezoelectric coefficient) as a function of La concentration (y). **c**, Evolution of the pseudocubic $\{200\}_{pc}$ XRPD Bragg profile of BF-PT45:La as a function of La concentration. The appearance of a third peak between the $(002)_T$ and $(200)_T$ peaks for $x \geq 0.27$ suggests an onset of a CL phase. **d**, Composition–temperature phase diagram of BF-PT45:La(y). The transition temperatures were obtained from temperature-dependent dielectric measurements (Supplementary Fig. 2) and high-temperature XRD measurements. a.u., arbitrary units; Temp, temperature.

carried out by La substitution as per the nominal formula $(1-x)$ $Bi_{1-y}La_yFeO_3$–$(x)PbTiO_3$. This choice was guided by the fact that La is known to induce domain miniaturization and improve the piezoelectric response in $Pb(Zr,Ti)O_3$ (ref. [15]). We synthesized a series of La-modified BF-PT ceramics by a conventional solid-state reaction technique (Methods and Supplementary Fig. 1). We explored the vast composition space (x,y) with $x > 0.30$ to retain the tetragonal structure with as much tetragonality as possible while being able to affect domain switching. After a series of experiments, we found that BF-PT with $x \geq 0.45$ can exhibit very large electrostrain values.

Electrostrain and correlation with global structure

Figure 1a shows the unipolar-field strain behaviour of $0.55Bi_{1-y}La_yFeO_3$–$0.45PbTiO_3$ (BF-PT45:La(y)) at a field amplitude of $80 kV cm^{-1}$ for different La concentrations (y). For $y < 0.20$, the electrostrain was very small and not measurable. A noticeable strain of 0.10% was seen for $y = 0.20$. The electrostrain rose to ~0.5% for $y = 0.25$ and to a very large value of 1.3% for $y = 0.30$. For $x = 0.32$, the electrostrain decreased slightly but was still very high (~1%). It collapsed to ~0.23% for $y = 0.35$ and became insignificant beyond this concentration. The reproducibility of the results was verified by repeated measurements on several samples across compositions. The critical composition $y = 0.30$ shows a large-signal piezoelectric coefficient d_{33}^* (S_{max}/E_{max} (S_{max}, maximum strain; E_{max}, maximum electric field)) of ~1,600 pm V^{-1} (Fig. 1b), the highest value ever reported in piezoceramics. Our electrostrain of 1.3% at $80 kV cm^{-1}$ is close to the record strain of 1.6% at the same field in a [001]-oriented single crystal of PZN-PT[2]. The non-saturating nature of electrostrain at $80 kV cm^{-1}$ suggests that it might still be possible to achieve electrostrain well beyond 1.3% on further increase of the field. We, however, could not realize this possibility because of the spontaneous fracture suffered by the piezoceramics due to the build-up of stress.

Figure 1c shows the evolution of the pseudocubic $\{200\}_{pc}$ X-ray powder diffraction (XRPD) Bragg profile of BF-PT45:La(y) as a function of La concentration (the full patterns are shown in the Supplementary Fig. 1). The tetragonality decreases from 0.14 at $y = 0.0$ (La free) to 0.023 at $y = 0.30$ (Supplementary Fig. 1b). For $x > 0.25$, a third peak appears between the two tetragonal peaks $(002)_T$ and $(200)_T$. This peak corresponds to a CL phase. The phase diagram, constructed using temperature-dependent dielectric

measurements (Supplementary Fig. 2), is shown in Fig. 1d. The significant enhancement of the electrostrain in the composition range $0.25 < y \leq 0.32$ has a strong correlation with the onset of the CL phase. The intensity of the CL peak decreases and that of the tetragonal peaks increases irreversibly after the application of a strong electric field (that is, poling), as shown in Fig. 2a. From a Rietveld analysis, we confirmed that the tetragonal fraction increased from 8% to 70%. The repeatedly obtained very large electrostrain of 1.3%, however, cannot be associated with this one-time irreversible CL-to-tetragonal transformation driven by an electric field (Supplementary Fig. 3).

To obtain a better insight into the nature of the field-driven CL → $P4mm$ transformation, we carried out Raman spectroscopy, transmission electron microscopy (TEM) and neutron powder diffraction (NPD) measurements on the unpoled and poled specimens of $y = 0.30$ (Fig. 2). Both the NPD patterns (marked by * in Fig. 2b) and the electron diffraction patterns (Fig. 2d,e) show superlattice reflections of the type ½{odd, odd, odd}$_{pc}$, which suggests cell doubling. The fact that the superlattice reflections are not visible in the XRPD patterns indicates that the structural distortion is primarily due to an antiphase oxygen octahedral tilt[16]. The true average structure of poled BF-PT:La($y = 0.30$) is therefore a superposition of antiphase tilted octahedra on the $P4mm$-like lattice distortion. The superlattice reflections are not present in the NPD pattern of the La-free composition of BF-PT, that is, the parent system ($y = 0$) (Supplementary Fig. 4 and Supplementary Table 1). In the framework of Glazer's tilt notation, antiphase tilts are possible in structures with the following space groups[16]: $I4/mcm$ (tilt system, $a^0a^0c^-$), $Imma$ ($a^0b^-b^-$), $R\bar{3}c$ ($a^-a^-a^-$), $C2/m$ ($a^0b^-c^-$), $C2/c$ ($a^-b^-b^-$) and $P\bar{1}$ ($a^-b^-c^-$). $R3c$ is ruled out because a rhombohedral structure cannot explain the splitting of the $\{200\}_{pc}$ in both the XRD and NPD patterns. We did not consider the triclinic $P\bar{1}$ structure. Superposition of the zone-centre Γ polar distortions with the different tilt models resulted in plausible structures in the $I4cm$, $Ima2$, $Imm2$, Cc, Cm and $C2$ space groups, in the order of decreasing symmetry (Supplementary Table 2)[17]. We fitted the NPD pattern of poled BF-PT45 ($y = 0.30$) with these structural models (Supplementary Fig. 5). The Cc model gave a distinct improvement as compared to the others (goodness of fit (χ^2) = 19.1 with $Imm2$, 17.2 with $Ima2$, 16.4 with $I4cm$ and 9.2 with Cc). From the refined coordinates (Supplementary Table 3), the octahedral tilt angle was estimated to be ~3.5°. The strong shift of Ti towards the pseudocubic [001] direction confirms that the polarization direction in the Cc structure is very close to pseudocubic $[001]_{pc}$ (Supplementary Fig. 6). The shortest Ti–O distance has increased from 1.71 Å for $y = 0$ (Supplementary Table 1) to 1.85 Å in $y = 0.30$ (Supplementary Fig. 6), which confirms that the decrease in the tetragonality with La substitution is associated with the decrease in the degree of the covalent character of the Ti–O bond.

Positional disorder

In contrast to the drastic changes seen in the XRPD and NPD patterns, we found no perceptible difference in the Raman spectra before and after poling (Fig. 2c). As Raman spectra probes structural coherence on a short length scale, this implies that on a shorter length scale the atomic configuration in the poled and unpoled BF-PT45:La($y = 0.30$) is nearly the same. That is, the structure of the unpoled $y = 0.30$ is also most likely to be Cc. The [100] zone axis high-angle annular dark-field scanning transmission electron microscopy (HAADF-STEM) images of the unpoled specimen revealed 90° domains of ~2–3 nm in size, which confirms the tetragonal-like distortion on the local scale (Fig. 3a and Supplementary Fig. 7). The c/a ratio estimated from the image within a nanodomain is ~1.02, a value close to the c/a obtained from the XRPD pattern of the poled sample. We also noted considerable positional disorder on the A site, which is common to other Pb- and Bi-based mixed perovskites[18]. The extent of the disorder was estimated by determining the precise A-site positions as the
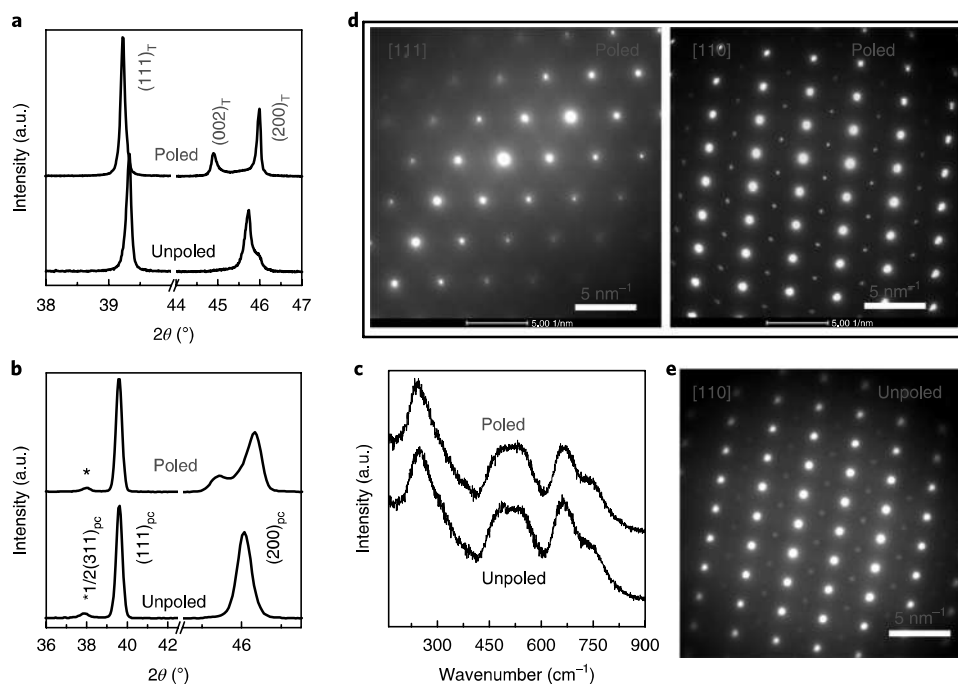
Fig. 2 | Structural study of poled and unpoled BF-PT45:La($y = 0.30$). a–e, XRD patterns (**a**), NPD patterns (**b**), Raman spectroscopy (**c**) and $\{111\}_c$ and $\{110\}_c$ zone electron diffraction patterns (**d,e**). The NPD patterns and [110] electron diffraction patterns show extra superlattice spots.

centre of a two-dimensional Gaussian fit to every A-site column in an image, followed by obtaining their standard deviation from an average structure. The positional disorder across several images in the unpoled specimen was found to be ~25 pm, and ~18 pm in the poled specimen (Fig. 3b,c). This confirms that the appearance of the CL phase in the XRPD pattern is associated with a large positional disorder. The random fields (induced by the La substitution in our case)[19] do not allow the long-range polarization/structural coherence to develop when the system is cooled in a zero-field state, as in relaxor ferroelectrics. We confirmed the relaxor ferroelectric nature of BF-PT45:La($y = 0.30$) (Supplementary Fig. 8). The application of a strong electric field in the non-ergodic state increases the coherence in regions sufficiently away from the random-field sites. In view of this, what appears as an electric-field-induced CL-to-tetragonal-like transformation in the XRPD is a case of the length-scale-dependent appearance of the different average structures. A length-scale-dependent average structure has also been reported in other ferroelectric alloys in recent years and appears to be a common phenomenon[20-22].
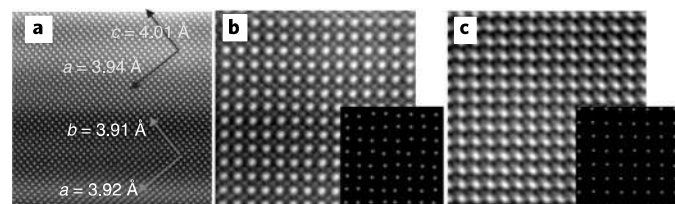

Fig. 3 | HAADFSTEM images of poled and unpoled BF-PT45:La($y = 0.30$).
a, Representative HAADF-STEM image of a [001]-oriented grain of unpoled BF-PT45:La($y = 0.30$). The region shows two different domains which confirms the presence of tetragonal distortion on a nanometre scale in the unpoled specimen. **b,c**, Magnified images of one domain in unpoled (**b**) and poled (**c**) specimens. The bright spots indicate the A-site (Pb/Bi/La) atoms in these images. The insets in **b** and **c** show the A-site centre-of-mass maps.

Electric-field-driven domain switching

We investigated the domain switching behaviour of BF-PT45:La($y = 0.30$) using XRD measurements in situ with an electric field. To establish a correlation with the measured unipolar electrostrain shown in Fig. 1a, we carried out diffraction measurements under a unipolar electric field on a poled pellet. Although we have proved that the most plausible structure of BF-PT45:La($y = 0.30$) is monoclinic Cc, for the interpretation of the XRD results, we assume the structure to be tetragonal like (as the XRD data originally suggested). The diffraction pattern of the poled pellet shows the pseudocubic $\{200\}_c$ profile to split into two tetragonal peaks $(002)_T$ and $(200)_T$ (Fig. 4a,b). The small peak between the $(002)_T$ and $(200)_T$ peaks corresponds to the remanent CL phase that survives after poling. The minor CL phase (~30%) is most likely to be regions near the strong random-field centres wherein the external field is incapable of developing the long-range tetragonal coherence. In a normal tetragonal ferroelectric perovskite, poling often increases the intensity of $(002)_T$ above that of $(200)_T$ due to the irreversible reorientation of the tetragonal domains[23]. Interestingly, this is not the case for BF-PT45:La($y = 0.30$) as the intensity ratio of $(002)_T$ and $(200)_T$ is very close to the value in the preferred orientation-free powder pattern. We estimated the extent of the domain switching fraction (η) using the equation[23]:

$$\eta_{002} = \frac{\frac{I_{002}}{I'_{002}}}{\frac{I_{002}}{I'_{002}} + 2\frac{I_{200}}{I'_{200}}} - \frac{1}{3}$$

where I_{002} and I_{200} are the integrated intensities of the $(002)_T$ and $(200)_T$ reflections, respectively, in the presence of the field. I'_{002} and I'_{200} are the integrated intensities of the $(002)_T$ and $(200)_T$ reflections, respectively, before the application of the field. After poling, the switched fraction was merely 0.10. With an increasing field, η_{002} increased again and reached a value of ~0.4 at 60 kV cm^{-1} and returned to 0.10 at $E = 0$ kV cm^{-1} (Fig. 4c). Interestingly, we found that the peak position of the residual CL phase shifts synchronously
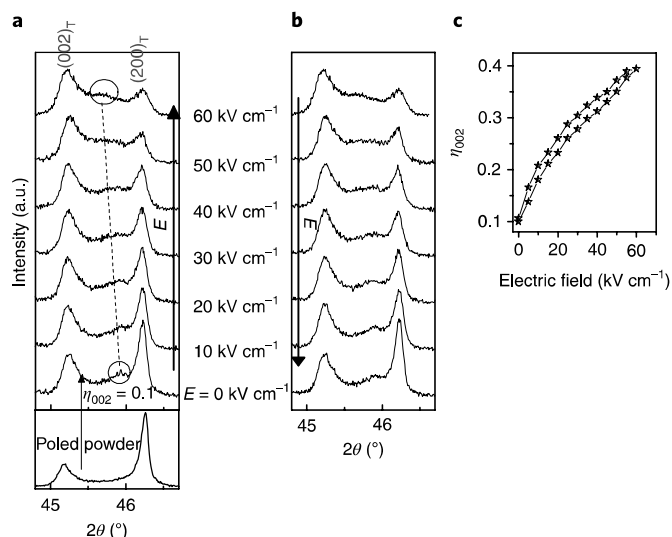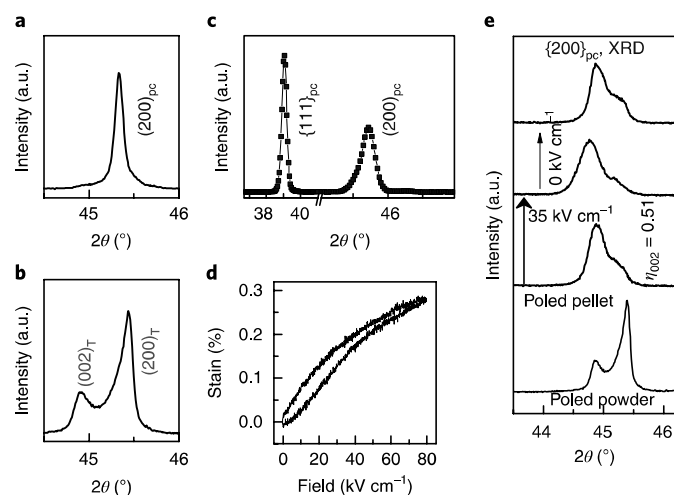
Fig. 4 | Domain switching with an electric field. a,b, The evolution of the $\{200\}_{pc}$ XRD Bragg profile of BF-PT:La($y=0.30$) as a function of increasing field (**a**) and decreasing field (**b**). The diffraction experiment was carried out on an initially poled pellet and an electric field was applied in the direction of the poling field to be consistent with the conditions of the unipolar electrostrain measurement shown in Fig. 1a. The peak between the two tetragonal peaks $(002)_T$ and $(200)_T$ corresponds to the CL phase. **c,** The domain-switching fraction (η_{002}) as a function of the cyclic unipolar field. The η_{002} starts from 0.10 at 0 field. This is because the first measurement ($E=0\,kV\,cm^{-1}$) is on a poled specimen that shows a remanent irreversible switching fraction of 0.10. For reference, the bottom panel of **a** shows the XRD profile of an untextured poled specimen (XRD on a powdered specimen of poled BF-PT45:La($y=0.30$)).

Fig. 5 | Comparison with PT-BNZ. a,b, XRD reflections of the pseudocubic $\{200\}_{pc}$ of unpoled (**a**) and of poled (**b**) PT-BNZ powder. **c,** Pseudocubic $\{111\}_{pc}$ and $\{200\}_{pc}$ NPD Bragg profiles of unpoled PT-BNZ powder. **d,** The unipolar strain in the corresponding sample. **e,** The domain switching in PT-BNZ from poled powder to poled pellet and then under a 35 kV cm⁻¹ field and after removal of the field. In contrast to the situation in BF-PT45:La($y=0.30$) (Fig. 4a), the poled specimen of PT-BNZ is heavily textured ($\eta \approx 0.5$). Further domain switching in the same direction is not significantly noticeable.

to a lower 2θ value as the switching fraction of the tetragonal domain increases with increasing field (Fig. 4a). This suggests a strong coupling between the two phenomena. On decreasing the field, the lattice strain of the CL phase relaxes and, by its coupling, forces the tetragonal domains to reverse switch (Fig. 4b). The minor CL phase therefore provides the necessary restoring force to reverse the tetragonal domain walls when the field is reduced. By taking into consideration the contribution of tetragonal domain switching and the lattice strain of the CL phase, the estimated electrostrain is very close to the observed value (Supplementary Table 4).

Comparison with an analogous system

For a better appreciation of the role of a large reverse domain switching in providing an enhanced electrostrain, we also carried out a comparative study of another analogous alloy system, $(1-x)PbTiO_3-(x)Bi(Ni_{1/2}Zr_{1/2})O_3$ (PT-BNZ). Similar to BF-PT45:La(y), PT-BNZ also exhibits a composition-driven tetragonal-to-CL transformation at $x \approx 0.44$ (ref. [24]) (Supplementary Fig. 9), and a poling-induced CL-to-tetragonal transformation (Fig. 5a,b). The critical composition of PT-BNZ, however, shows an electrostrain of ~0.3% at 80 kV cm⁻¹ (Fig. 5d). This value is merely one-quarter the extraordinarily large electrostrain shown by BF-PT45:La($y=0.30$). Although the low electrostrain in PT-BNZ can partly be rationalized by arguing that the tetragonality of PT-BNZ (c/a −1 of ~0.011) is nearly half the tetragonality in BF-PT45:La($y=0.30$) (c/a −1 of ~0.023), what is important is the lack of reverse domain switching in the former (Fig. 5e). After poling, the irreversibly switched fraction of the tetragonal domains is 0.50 (Fig. 5e), which is significantly larger than that in BF-PT45:La($y=0.30$) ($\eta=0.10$). This considerably lessens the scope for additional domain switching on the application of a field in the same direction, as evident from Fig. 5e. Note, in passing, that the large

difference in the electrostrains of BF-PT:La and PT-BNZ cannot be attributed to the difference in the grain size of the specimens, as both specimens exhibit grain size in the range 6–8 μm (Supplementary Fig. 10). The low symmetry (Cc) of the ferroelectric phase may aid to the efficient domain switching in BF-PT45:La($y=0.30$) as it allows more domain variants to appear, which in turn increases the probability of finding compatible variants across neighbouring grains for an efficient collective switching to take place across the piezoceramic body[5]. In contrast, the ferroelectric phase of PT-BNZ has a higher symmetry ($P4mm$), and there was no evidence of superlattice reflections that corresponded to octahedral tilt in the NPD pattern (Fig. 5c). We also found that the large reverse switching in BF-PT:La is robust as the electrostrain did not decrease after repeated cycling in excess of 10⁴. In contrast, the electrostrain of PT-BNZ decreased after 100 cycles (Supplementary Fig. 11).

Unique structural features of the critical composition

Next we discuss the factors that make BF-PT45:La($y=0.30$) unique as compared to other compositions in the large composition space (x,y) of $(1-x)Bi_{1-y}La_yFeO_3-(x)PbTiO_3$. Figure 6a shows the evolution of the XRPD pattern of $0.60Bi_{1-y}La_yFeO_3-0.40PbTiO_3$ (BF-PT40:La(y)) as a function of La concentration. Here the structure evolves from tetragonal ($y=0$) to rhombohedral ($y=0.20$), as confirmed by the splitting of $\{111\}_{pc}$. We found that all BF-PT:La with $x<0.45$ showed the same structural evolution with La concentration. In contrast, for all $x\geq0.45$, the tetragonal structure transforms to CL with increasing La concentration (Fig. 1c). The second important difference is that, after poling, the rhombohedral composition BF-PT40:La($y=0.20$) exhibits no further change in structure on the global scale (Fig. 6b), whereas the CL phase of BF-PT45:La($y=0.30$) transforms to a tetragonal majority (Fig. 2a). Thus, all La-modified $(1-x)BF-(x)PT$ with $x<0.45$ behave like a normal ferroelectric that exhibits a large irreversible domain switching (less reverse switching) after poling. It is therefore not surprising that BF-PT40:La($y=0.20$) shows an electrostrain of ~0.22% at 80 kV cm⁻¹ (Fig. 6c). Other groups have also reported electrostrain values in the same range on similar compositions[25,26].
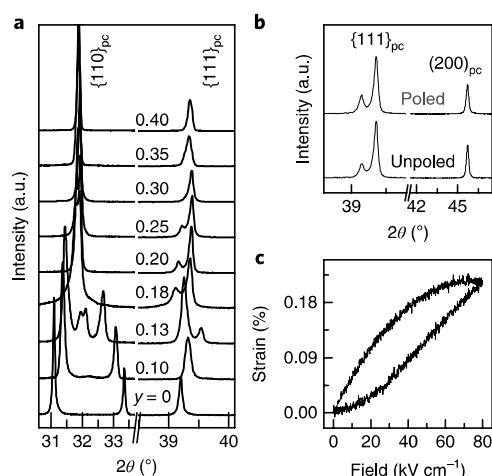
Fig. 6 | Structure–property correlation in 0.60Bi$_{1-y}$La$_y$FeO$_3$–0.40PbTiO$_3$.
a, The evolution of the XRPD pattern of 0.60Bi$_{1-y}$La$_y$FeO$_3$–0.40PbTiO$_3$ as a function of La concentration (y). **b**, Pseudocubic $\{111\}_{pc}$ and $\{200\}_{pc}$ XRD reflections of the poled and unpoled powder 0.60Bi$_{1-y}$La$_y$FeO$_3$–0.40PbTiO$_3$ (y = 0.20). **c**, Unipolar electrostrain response in the corresponding sample.

Outlook

Our results suggest that the morphotropic phase boundary systems, well known for their enhanced weak-signal piezoelectric response (d_{33}), may not be the right candidates to achieve a very large electrostrain in polycrystalline piezoceramics as they do not normally show a large reverse switching of the ferroelectric–ferroelastic domains. This property should rather be sought in ferroelectric systems that exhibit the polarization of short and long coherence lengths, and a strong coupling between them. Based on the present study, we argue that design criterion for the development of large-strain actuator materials should start with the selection of a ferroelectric host that exhibits a large spontaneous polarization/strain, and then find a suitable chemical substituent that not only brings about a heterogeneous domain structure in the context stated above but is also capable of lowering the symmetry of the ferroelectric phase.

Methods

Methods, including statements of data availability and any associated accession codes and references, are available at https://doi.org/10.1038/s41563-018-0060-2.

References

1. Uchino, K. *Piezoelectric Actuators and Ultrasonic Motors* (Kluwer Academic, Boston, 1996).
2. Park, S.-E. & Shrout, T. R. Ultrahigh strain and piezoelectric behavior in relaxor based ferroelectric single crystals. *J. Appl. Phys.* **82**, 1804–1811 (1997).
3. Du, X., Belegundu, U. & Uchino, K. Crystal orientation dependence of piezoelectric properties in lead zirconate titanate: theoretical expectation for thin films. *Jpn J. Appl. Phys.* **36**, 5580–5587 (1997).
4. Hall, D. A., Steuwer, A., Cherdhirunkorn, B., Mori, T. & Withers, P. J. Analysis of elastic strain and crystallographic texture in poled rhombohedral PZT ceramics. *Acta Mater.* **54**, 3075–3083 (2006).
5. Li, J. Y., Rogan, R. C., Üstündag, E. & Bhattacharya, K. Domain switching in polycrystalline ferroelectric ceramics. *Nat. Mater.* **4**, 776–781 (2005).
6. Liu, X. & Tan, X. Giant strains in non-textured (Bi$_{1/2}$Na$_{1/2}$)TiO$_3$-based lead-free ceramics. *Adv. Mater.* **28**, 574–578 (2016).
7. Damjanovic, D. Ferroelectric, dielectric and piezoelectric properties of ferroelectric thin films and ceramics. *Rep. Prog. Phys.* **61**, 1267–1324 (1998).
8. Jones, J. L., Hoffman, M., Daniels, J. E. & Studer, A. J. Direct measurement of the domain switching contribution to the dynamic piezoelectric response in ferroelectric ceramics. *Appl. Phys. Lett.* **89**, 092901 (2006).
9. Fu, H. & Cohen, R. E. Polarization rotation mechanism for ultrahigh electromechanical response in single-crystal piezoelectrics. *Nature* **403**, 281–283 (2000).
10. Wada, S., Park, S.-E., Cross, L. E. & Shrout, T. R. Domain configuration and ferroelectric related properties of relaxor based single crystals. *J. Kor. Phys. Soc.* **32**, S1290–S1293 (1998).
11. Ren, X. Large electric-field-induced strain in ferroelectric crystals by point defect mediated reversible domain switching. *Nat. Mater.* **3**, 91–94 (2004).
12. Xu, G., Zhong, Z., Bing, Y., Ye, Z.-G. & Shirane, G. Electric-field-induced redistribution of polar nano-regions in a relaxor ferroelectric. *Nat. Mater.* **5**, 134–138 (2006).
13. Fedulov, S. A., Ladyzhinskii, P. B., Pyatigorskaya, I. L. & Venevetsev, Yu. N. Complete phase diagram of the PbTiO$_3$–BiFeO$_3$ system. *Sov. Phys. Solid State* **6**, 375–378 (1964).
14. Comyn, T. P. et al. Phase-specific magnetic ordering in BiFeO$_3$–PbTiO$_3$. *Appl. Phys. Lett.* **93**, 232901 (2008).
15. Dai, X., Xu, Z. & Viehland, D. J. Normal to relaxor ferroelectric transformations in lanthanum-modified tetragonal structured lead zirconate titanate ceramics. *J. Appl. Phys.* **79**, 1021–1026 (1996).
16. Howard, C. J. & Stokes, H. T. Group-theoretical analysis of octahedral tilting in perovskites. *Acta Cryst.* **B54**, 782–789 (1998).
17. Stokes, H. T., Kisi, E. H., Hatch, D. M. & Howard, C. J. Group-theoretical analysis of octahedral tilting in ferroelectric perovskites. *Acta Cryst.* **B58**, 934–938 (2002).
18. Grinberg, I., Cooper, V. R. & Rappe, A. M. Relationship between local structure and phase transitions of a disordered solid solution. *Nature* **419**, 909–911 (2002).
19. Westphal, V., Kleeman, W. & Glinchuk, M. D. Diffuse phase transitions and random-field-induced domain states of the relaxor ferroelectric PbMg$_{1/3}$Nb$_{2/3}$O$_3$. *Phys. Rev. Lett.* **68**, 847–850 (1992).
20. Rao, B. N. et al. Local structural disorder and its influence on the average global structure and polar properties in Na$_{0.5}$Ba$_{0.5}$TiO$_3$. *Phys. Rev. B* **88**, 224103 (2013).
21. Usher, T.-M. et al. Local and average structures of BaTiO$_3$–Bi(Zn$_{1/2}$Ti$_{1/2}$)O$_3$. *J. Appl. Phys.* **120**, 184102 (2016).
22. Ihlefeld, J. F. et al. Scaling effects in perovskite ferroelectrics: fundamental limits and structure–property relations. *J. Am. Ceram. Soc.* **99**, 2537–2557 (2016).
23. Pramanick, A., Damjanovic, D., Daniels, J. E., Nino, J. C. & Jones, J. L. Origins of electro-mechanical coupling in polycrystalline ferroelectrics during subcoercive electrical Loading. *J. Am. Ceram. Soc.* **94**, 293–309 (2011).
24. Rong, Y. et al. Large piezoelectric response and polarization in relaxor ferroelectric PbTiO$_3$–Bi(Ni$_{1/2}$Zr$_{1/2}$)O$_3$. *J. Am. Ceram. Soc.* **96**, 1035–1038 (2013).
25. Cheng, J.-R., Eitel, R. & Cross, L. E. Lanthanum-modified (1–x)(Bi$_{0.8}$La$_{0.2}$)(Ga$_{0.05}$Fe$_{0.95}$)O$_3$–xPbTiO$_3$ crystalline solutions: novel morphotropic phase-boundary lead-reduced piezoelectrics. *J. Am. Ceram. Soc.* **86**, 2111–2115 (2003).
26. Leist, T., Granzow, T., Jo, W. & Rödel, J. Effect of tetragonal distortion on ferroelectric domain switching: a case study on La doped BiFeO$_3$–PbTiO$_3$ ceramics. *J. Appl. Phys.* **108**, 014103 (2010).

Author contributions

R.R. conceived the work, participated in planning the experiments and in the interpretations of the data. B.N., J.S.M. and R.P. prepared the specimens and carried out the characterization and data analysis. P.N. and B.D. carried out the HRTEM experiments and analysis. K.Y. did the TEM sample preparation and electron diffraction. A.S. provided the NPD data.

Competing interests

The authors declare no competing interests.

Methods

Piezoceramics of $(1-x)Bi_{1-y}La_yFeO_3-xPbTiO_3$ were prepared by a conventional solid-state sintering technique using analytical grade high-purity powders of Bi_2O_3, PbO, Fe_2O_3, TiO_2 and La_2O_3 (Alfa Aesar, purity >99.5%). We also added 0.2 wt% of MnO_2 to reduce the leakage current. After calcination at 800 °C for 2 h, the uniaxially pressed pellets were sintered in the range (depending on the composition) 950–1,100 °C for 2 h amid a sacrificial powder of the same composition to minimize the volatilization of PbO and Bi_2O_3. Similarly, a series of (x)BNZ-$(1-x)$PT was prepared in the composition range $0.38 \leq x \leq 0.44$ by a conventional solid-state synthesis technique. Dried reagent grade oxides of Bi_2O_3, PbO, NiO, ZrO_2 and TiO_2 (Alfa Aesar, purity >99.5%) were mixed according to stoichiometric formulas of each composition. The pellets were sintered in the range 1,100–1,150 °C for 3 h. XRPD studies were performed with a Rigaku (SmartLab) rotating-anode-based diffractometer with Cu Kα radiation working in the Bragg–Brentano reflection geometry. The diffraction patterns of 'unpoled specimens' were obtained by grinding the sintered pellets to powder and subsequent annealing at ~700 °C for 1 h to remove stress-induced ferroelastic changes in the specimens, if any, incurred during the grinding process. The XRD patterns of the poled specimens were collected after grinding the poled pellets to powder. XRD experiments in situ with an electric field were carried out on pellets. Very thin gold electrodes were sputter deposited across the opposite faces of a circular pellet and XRD data were collected from one face while the field was held constant. In this geometry, the planes that contributed to the observed Bragg peaks were those ones parallel to the pellet surface (or nearly perpendicular to the applied field). NPD

experiments were carried out at the SPODI diffractometer at FRM II, Germany, using a wavelength of 1.548 Å. Rietveld refinement was carried out using the program FULLPROF[27]. Microstructural features of the pellets were examined by scanning electron microscopy (FEI, Quanta 200). Ferroelectric and electrostrain measurements were carried out with a Radiant Precision Premier II loop tracer and an MTI photonic sensor, respectively. Dielectric measurements were carried out on fired-on silver-electroded circular discs of ~1 mm thickness and ~10 mm diameter. High-resolution transmission electron microscopy (HRTEM) on a C_s-corrected Titan G2 microscope operated at 200 kV. Electron-transparent samples were prepared both in the unpoled and poled states via conventional mechanical polishing followed by ion milling. Reciprocal space analysis was performed by obtaining selected area electron diffraction patterns of regions (~100 nm diameter) along various zones. Real-space analysis was performed on atomic resolution images obtained via HAADF-STEM. Chemical maps were obtained using energy dispersive spectroscopy in a ChemiSTEM set-up (four solid-state detectors placed symmetrically about the optical axis) with simultaneous HAADF-STEM imaging.

Data availability. All data generated and analysed during this study are available in the paper and its Supplementary Information. Extra data can be obtained from the corresponding authors on request.

References

27. Carvajal, J. R. *FULLPROF. A Rietveld refinement and pattern matching analysis program* (Laboratories Leon Brillouin (CEA-CNRS), France, 2000).